Research Article | Vol. 33, No. 15 / 28 Jul 2025 / Optics Express 31701
Optics EXPRESS

Hole-based stealthy hyperuniform semiconductor computational metamaterials for the mid-infrared

MANUEL GALLEGO,[1,*] SARA KACMOLI,[1,2] YEZHEZI ZHANG,[1,3] MICHAEL A. KLATT,[4,5,6] AND CLAIRE F. GMACHL[1]

[1]Department of Electrical and Computer Engineering, Princeton University, Princeton, NJ 08544, USA
[2]Omenn-Darling Bioengineering Institute, Princeton University, Princeton, NJ 08544, USA
[3]Current address: Cruise LLC, 333 Brannan St., San Francisco, CA 94107, USA
[4]German Aerospace Center (DLR), Institute for AI Safety and Security, Wilhelm-Runge-Str. 10, 89081 Ulm, Germany
[5]German Aerospace Center (DLR), Institute of Frontier Materials on Earth and in Space, Functional, Granular, and Composite Materials, 51170 Cologne, Germany
[6]Department of Physics, Ludwig-Maximilians-Universität München, Schellingstr. 4, 80799 Munich, Germany
*mg6693@princeton.edu

Abstract: Stealthy-hyperuniform heterostructures are metamaterials with the potential for optical image processing at angles away from normal incidence. They show analogous properties to photonic crystals while circumventing the spatial anisotropy which often hinders the latter's use. In this paper, we have designed, fabricated, and characterized a hole-based stealthy-hyperuniform structure on a quantum cascade layer substrate. The infrared spectral data reveal a sizable gap-midgap ratio of 10.4% for a photonic band gap around ~12.0 μm in the form of an enhanced reflection region for increasing incidence angles. The stealthy hyperuniform metamaterial also showed spatial isotropy by its unchanging reflection spectrum for all in-plane rotational angle measurements.

1. Introduction

Disordered hyperuniform structures can form a type of metamaterial with inherent hidden order [1]. Hyperuniform point distributions were originally discovered by Torquato and Stillinger in a systematic characterization of local density fluctuations [1]. These point distributions can create an exotic state of matter that combines properties from both liquids and crystals that manifest as hidden order within the structure. [2–10]; most notably, recent work indicated that so-called stealthy hyperuniform (SHU) heterostructures are the only disordered systems that show a complete photonic band gap (PBG) in the thermodynamic limit [2,11,12] (number of points growing to infinity). Initially, PBGs have been thought to be exclusive to ordered structures such as photonic crystals and quasicrystals [13,14]; however, through a powerful collective-coordinate optimization technique [4,12,15–17], it is possible to engineer a SHU structure with targeted structure factor [18,19].

SHU point patterns [15,17] are a subclass of hyperuniform point distributions, in which the structure factor (an order parameter) vanishes below a critical wave vector, k_c. Hyperuniform point distributions (including stealthy) also have vanishing density fluctuations in the infinite wavelength limit [11]. Additionally, the disordered nature of the pattern makes SHU devices spatially isotropic while retaining a PBG, as opposed to their photonic crystal counterparts that also possess PBGs, but are anisotropic from their spatial symmetries. These unique properties of SHU structures have enabled applications in optics and photonics such as the fabrication of disordered silicon photonic waveguides [20], mode selection in THz quantum cascade lasers

#559370 https://doi.org/10.1364/OE.559370
Journal © 2025 Received 24 Feb 2025; revised 24 May 2025; accepted 2 Jul 2025; published 21 Jul 2025

Optics EXPRESS

(QCLs) [21], tailored light scattering [22], disordered lenses [23], and others [24–28]. An application of special interest is the potential to use such structures as computational metamaterials for image edge detection. PBGs in photonic crystals have been shown to be capable of performing image differentiation [29,30]. However, they are constrained to normal incidence, and suffer from the anisotropy of the crystal structure. In contrast, PBGs in SHU structures appear at larger angles away from normal incidence while also being spatially isotropic as previously mentioned.

Digital image processing in contemporary computing requires effective ways of performing edge detection [31]; with applications in medicine [32], self-driving vehicles [33], facial recognition [34], etc. Computer vision algorithms are capable of calculating the edges of an image in a great variety of ways [35], with the simplest being a convolution operation using a Laplacian filter (kernel) [31]. However, some applications demand real-time edge detection in which digital image processing is not suitable. Traditional real-time optical image processing is done with Fourier optics; in the case of edge detection, a 4F system is used. A 4F setup requires precise alignment of optical components and only functions at normal incidence. Additionally, the optical image processing is constrained to transmission mode only. SHU metamaterials have the potential to circumvent some of these constraints while still delivering useful real-time object edge information [3].

In this work, we first focus on a mid infrared imaging application, we compute, design, and test a classical Fourier optical image processing setup for edge detection in the mid-IR using a 9 μm QC laser source (Daylight Solutions laser), a 4F correlator system of ZnSe lenses, and an IR camera. All components are placed equidistant, and the beam spot aligned on the surface of a triangle mask aperture. The triangle outline of the mask is observed on the IR camera detector plane. We then focus on the nature of SHU structures by demonstrating a SHU pattern on a QC-layered semiconductor substrate using etched holes. The size of the pattern unit cell is 30 μm x 30 μm, with an average center to center point distance of 3 μm; this unit cell is then tiled across a 1 cm^2 sample. The designed PBG is located at 12.3 μm, and we indeed observe the PBG at 12.0 μm using a broadband IR source. We also observe the spatial isotropy of the SHU pattern by rotating it about its own plane at a fixed incidence angle.

2. SHU simulations

A point distribution is *hyperuniform* if the variance of the number of points in an observation window of radius R grows asymptotically slower than the area of the window itself. This definition equates to a structure factor $S(k)$ of zero for $k \to 0$, where k is the wavevector in reciprocal space [1,2].

We use a SHU point pattern from Florescu et al 2009 (Fig. 1(b)), consisting of 100 points within a 30 μm square unit cell, and order parameter of $\chi = 0.49$. For this stealthy pattern, there exist a discrete region of no scattering a near the origin [2] in reciprocal space (Fig. 1(c)); consistent with the expected behavior of stealthy hyperuniform structures. We compute the photonic band structure with the electromagnetic mode solver (MPB) [36], which uses harmonic mode solutions to Maxwell's equations. Our hole-based SHU semiconductor metamaterial was modeled as a periodic geometry consisting of air holes with infinite depth in a material with dielectric constant of $\varepsilon = 10.6$. This value corresponds to indium phosphide with quantum cascade epilayers, matching the material properties of the QC wafer substrate used in this study.

Similarly, a triangular photonic crystal (Fig. 1(a)) with lattice constant $a = 3$ μm was modeled for a comparison of isotropy. The lattice constant was selected to match the average point distance in the SHU pattern. The SHU pattern is comprised of a square unit cell that is tiled and fills the entire computational domain, so the Brillouin zone by consequence is that of the square lattice. The mode solver operates by computing the associated frequencies and bands along the edges of the Brillouin zone, allowing us to construct band diagrams highlighting the existence, or lack thereof, of a PBG (Fig. 2(b)). Since our SHU unit cell is rather small (102 points) we compute

Optics EXPRESS

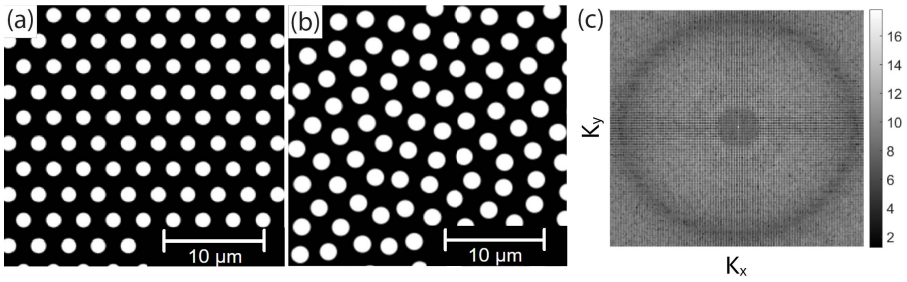

Fig. 1. (a) Hexagonal photonic crystal hole pattern with lattice constant a = 3 μm and hole diameter of 1.5 μm, (b) one unit cell of the SHU hole pattern with hole diameter of 2.2 μm and average center to center hole spacing of 3 μm. (c) K space transform of the SHU point pattern in (b). The dark circle region near the center correspond to regions with no scattering [2].

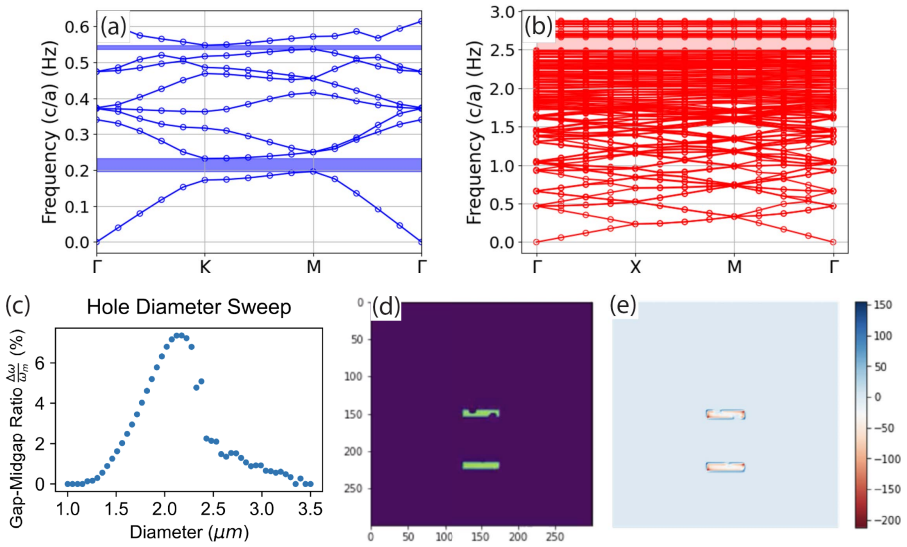

Fig. 2. (a) TE band diagram of the hexagonal hole photonic crystal used for reference (b) TE band diagrams of the SHU hole pattern. Around 110 individual bands were calculated to observe the SHU pattern band gap at around 2.4 (c/a) Hz, i.e. 12.3 μm wavelength. c is the speed of light in vacuum, and a = 30 μm is the size of the unit cell. (c) PBG simulation sweep of various diameters for the SHU hole pattern showing largest values near 2.2 μm, and the percolation of the holes as the diameter grows larger. (d) FDTD simulation in MEEP of an electric field source with two rectangular blocks as the input image. (e) Shows the processed output after passing through a pillar based SHU structure with a 40% PBG centered around 8 μm. The electric field emphasizes the edges of the image by outlining the rectangular block [3].

the photonic bands over the entire first irreducible brillouin zone domain. Starting from the center Γ point, to the X and M points, and folding back onto the center.

We computed the in plane (K_z = 0) band diagrams, in both transverse electric (TE) and transverse magnetic (TM) polarizations. TE polarization is perpendicular to the incidence plane of the SHU sample, and TM is parallel. In the case of our SHU hole geometry, the PBG appears in TE polarization but not in TM (if the geometry were to be inverted to dielectric pillars in air, then the PBG would appear in the TM polarization but not in TE [3]). For a SHU pattern with

Optics EXPRESS

2.2 μm diameter holes and 3 μm average point distance, the TE band gap was computed to be centered at approximately 12.3 μm (810 cm^{-1}) with 7.0% width, as shown in Fig. 2(b). The diameter of the holes was optimized by simulating and selecting the largest gap-midgap ratio from a range (1.0 - 3.5 μm) of diameters, as illustrated in Fig. 2(c). The minimum and maximum ranges are constrained by the smallest possible fabrication requirements, and the overlapping (percolation) of holes, respectively. Hole diameters from 1.8 - 2.2 μm were found to be best, leading to a 5 - 7% wide PBG.

Successfully verifying that our SHU structure, comprising air holes in a semiconductor, exhibits a PBG allows us to investigate its potential for edge detection. Previous work [29] has demonstrated that photonic crystal slabs can perform edge detection by acting as a Laplacian operator ($\nabla^2 = \partial_x^2 + \partial_y^2$) for normal incident light. In this context, the incoming transverse electric field $E_{in}(x, y)$ is transformed to $E_{out} = \nabla^2 E_{in}(x, y)$. In reciprocal Fourier space, this is equivalent to an isotropic quadratic image transfer function of the following form:

$$t(k_x, k_y) = \begin{pmatrix} a_s({k_x}^2 + {k_y}^2) & 0 \\ 0 & a_p({k_x}^2 + {k_y}^2) \end{pmatrix} \tag{1}$$

Where a_s and a_p denote the different polarization directions [3,29].

Torquato has shown in their study of hyperuniformity that it is possible to engineer hyperuniform distributions with targeted structure factors [2]. Specifically, SHU patterns with structure factor in a power-law form of $S(k) = |k|^\alpha$ for small wavenumbers and α>0. In our study, a SHU pattern with a structure factor in the form of $S(k) = |k|^2$ reflects the isotropic quadratic transfer function needed to perform the edge detection computation [3].

In previous studies [3], we performed finite-difference time-domain (FDTD) simulations of our SHU structures, as shown in Fig. 2(d), 2(e). In this simulation, the source electric field are rectangular blocks that act as the input image, upon which the SHU structure operates. The SHU point distribution is the same, however the geometry is inverted to create tall pillars of semicondutor surrounded by air. This pillar based SHU exhibits a PBG of approximately 40%, spanning from 6.6 μm to 9.1 μm, and centered around 8 μm. Figure 2(e) shows the processed image after the light passes through SHU. The electric field amplitude is strongly concentrated along the perimeter of the rectangular block, clearly emphasizing the input image edges.

3. 4F correlator edge detection

Classical image processing involves applying a Fourier transform, and modulating the input image. In the case of edge detection, a high-pass filter is used to block low-frequency components in the Fourier transformed image; leaving only the high-frequency components corresponding to the edges. Classical edge detection can be performed using a 4F correlator consisting of the object, a pair of lenses, and the image plane; their placement determined by the focal lengths of the lenses, and each component positioned one focal length apart.

At its core, the 4F system works by focusing and modulating a diffraction pattern. The first lens effectively performs a Fourier transform of the input image, turning the focal plane into the Fourier plane. Placing a filter mask in the focal plane can selectively block specific spatial frequencies, producing different optical effects. Low spatial frequencies near the bright center spot are associated with image blur (low-pass filter), while high spatial frequencies are associated with the edges (high-pass filter).

Using MATLAB, we performed the edge detection computation on an input triangular mask (Fig. 3(a)) using the isotropic quadratic transfer function in Eq. (1), which in real space corresponds to the applying the convolution between a Laplacian kernel and the mask. In reciprocal space, this computation is performed by simply multiplying the quadratic transfer function with the

Optics EXPRESS

fourier tranformed image data of the illuminated mask. As expected, the output processed image in Fig. 3(c) highlights the edges of the triangle, corresponding to regions of high contrast.

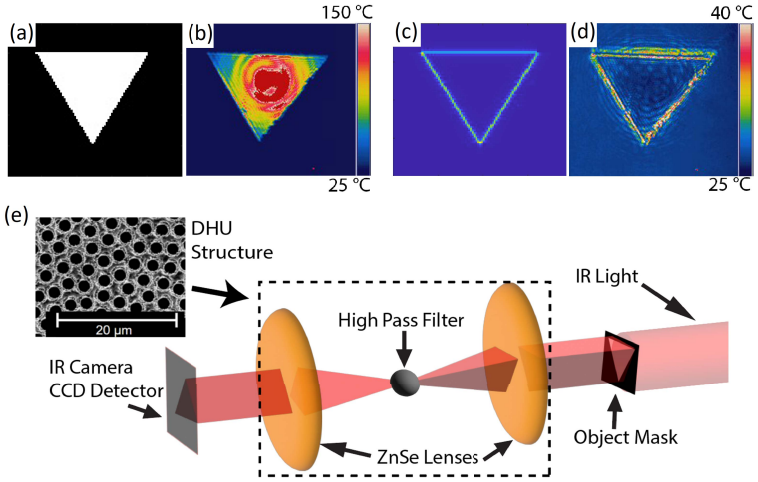

Fig. 3. (a) shows the input triangular geometry used in MATLAB for digital image processing, and (b) FLIR (proper noun) IR camera picture of the illuminated copper mask in the 4F correlator imaging setup. In MATLAB the convolution between the image and a Laplacian filter is performed by taking the multiplication of the image's and filter's Fourier transforms. The resulting digital image highlights the edges of the input as shown in (c). In the imaging setup, the illuminated mask image is focused onto the focal plane of the first lens, and modulated using a high pass filter. The high frequency components associated with the edges of the mask are then imaged onto the FLIR IR camera detector as shown in (d). A schematic of the setup with the 4F correlator is shown in (e). The boxed region (4F system) corresponds to the components that could potentially be replaced by a fabricated SHU structure to perform image differentiation analogous to the classical Fourier optical system.

Next, we aimed to compare our simulation results to traditional Fourier optics based edge detection methods. The experimental setup uses a pulsed 9 μm external cavity quantum cascade laser, reflecting off a parabolic mirror to expand the beam and illuminate the mask at the object plane. The 4F system consists of two 1.5" focal length lenses, and a metal ball serving as a high pass filter. Lastly, an IR camera is positioned at the image plane to capture the filtered image. The camera operates at at a slow frame rate of 30 frames per second which is significantly slower than the laser pulse frequency, resulting in an averaged image.

To match with the triangle geometry from the MATLAB computation, the object mask consists of a triangular opening cut into an opaque copper sheet, with an area of approximately 4 mm^2. Figure 3(b) shows the fully illuminated the mask where there is significant temperature difference between the beam's center and the surrounding mask. This enhances the image contrast and emphasizes the edge detection when applying the high-pass filter on the Fourier plane. Figure 3(d) shows the processed image of the mask at the object plane modulation. The contrast is reduced, as most of the light is blocked by the filter, while the highlighted edges and ripples in the temperature profile correspond to the Fourier magnitude and phase components of the object, respectively. The boxed region in Fig. 3(e) highlights the components of the 4F system which could potentially be replaced by the SHU structure; while keeping the rest of the setup. The SHU pattern has the potential to extract the edges of an image when the frequency of the source matches, or resonates with, the center frequency of the designed SHU PBG [3].

Optics EXPRESS

4. Device fabrication

The SHU samples consist of the same pattern shown in Fig. 2(b) tiled across a 1 cm^2 substrate. The hole diameters of the samples we fabricate vary from 0.9 - 2.1 μm, and 3 μm average distance between centers. In addition, an unpatterned sample, and a hexagonal photonic crystal with 3 μm lattice constant and 1.5 μm hole diameter were also fabricated for reference (Fig. 4(a), 4(b)). All samples are fabricated on an InP substrate with epitaxially-grown QC layers for potential future integration with QCL systems. However, any high index substrate platform will see the same results. The device fabrication involves standard optical photolithography and reactive ion etching (RIE). The deep etching of the semiconductor layers is performed using Cl_2 and BCl_3 chemistry at high temperatures (220° C) [37]. For this reason, we use a SiO_2 hard mask patterned via direct-write lithography as opposed to a more common photoresist mask. Our process is developed to achieve smooth and vertical sidewalls both in the hard mask and the semiconductor itself. The holes are etched deep through the active core of the QC device and into the bottom cladding region (Fig. 4(c)) to a total depth of about 5.5 μm. Lastly, we cleave the sample, and lap and polish it down to about 250 μm thick for increased transmission. To prepare for measurements, the samples are mounted to a copper block and placed in a custom-built rotational mount.

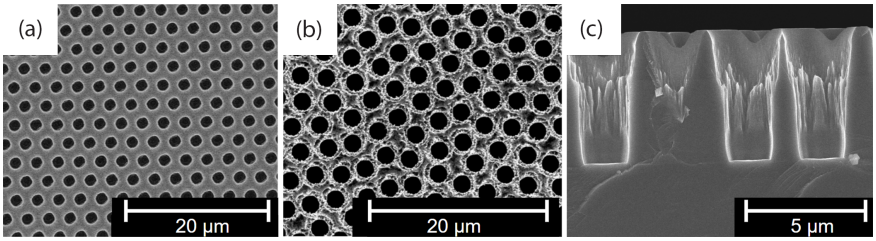

Fig. 4. Scanning electron microscopy (SEM) images of (a) the top view of the hexagonal photonic crystal, (b) the top view of the SHU sample with hole diameter of 1.8 μm, and (c) and the cross section of the SHU sample holes with a depth of about 5.5 μm. The surface roughness visible in (b) and (c) is primarily due to mask erosion from the etch step. However this is not expected to affect measurements since the roughness is significantly smaller than the wavelengths used.

5. Experimental setup

To conduct a thorough study of transmission and specular reflection spectra, a setup outside of the Fourier Transform Infrared (FTIR) Spectrometer is created and shown in Fig. 5. It consists of the globar source inside the FTIR, an external cryogenically cooled mercury cadmium telluride (LN_2-MCT) photodetector, three rotational stages to adjust sample and detector angles, and a polarizer. The collimated light from the FTIR first passes through a set of focusing ZnSe lenses, and then through a wire grid polarizer to select between TE or TM modes. The sample is mounted on a 3D printed rotational mount and placed at the focal point of the focusing lenses. The rotational mount can vary the incidence angle on the sample surface, as well as rotate about its own in-plane axis for in-plane rotational angle measurements. The set-up is designed to work in both transmission and reflection mode allowing rays away from normal incidence to pass unobstructed. Reflection mode is measured as specular reflection since this is where the majority of the signal is detected. Additionally, the effect of the PBG is more evident at larger incidence angles as more of the light is able to be guided parallel to the surface of the SHU structure. The photodetector used in this set up is a LN_2-MCT detector that rotates around the sample on a

Optics EXPRESS

swiveling arm. Two apertures are mounted in front of the photodetector to reduce oversampling, followed by another ZnSe lens to focus the light onto the surface of the photodetector.

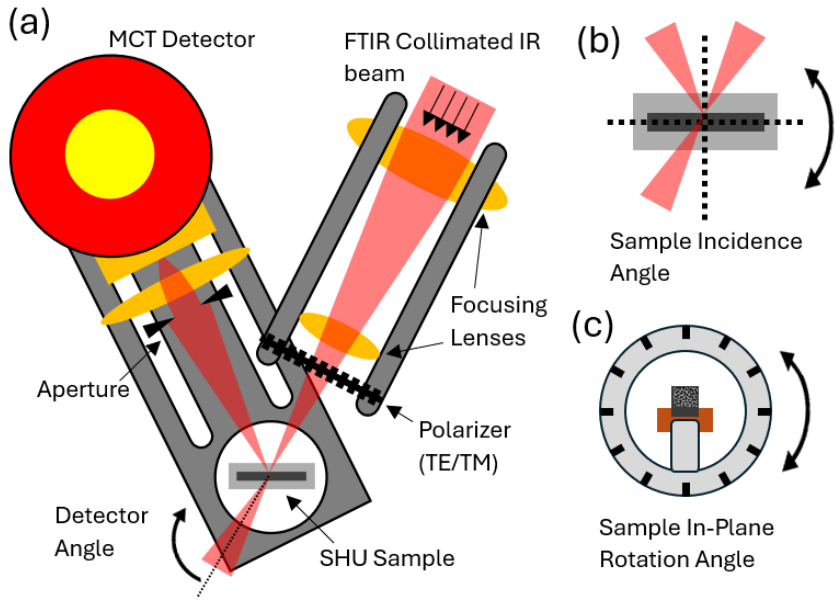

Fig. 5. (a) Experimental setup to measure transmission and specular reflection IR spectra of the fabricated SHU samples. On the right side, the collimated IR beam from the FTIR passes through a set of focusing lenses and a polarizer. The IR beam is focused onto the sample surface and the polarization is adjusted for TE or TM measurements. On the left side of the setup, the light passes through an aperture, followed by a focusing lens, and finally an MCT liquid nitrogen cooled detector. The detector setup rotates to perform either transmission or reflection measurements as needed. The sample is held on a 3D printed mount (b, c) that can rotate to change the angle of incidence of the incoming light, as well as rotate along in the sample plane for in-plane angle resolved measurements.

6. Infrared spectrum analysis

A background spectrum was recorded for all measurements to eliminate atmospheric features, such as H_2O and CO_2 absorption peaks, from the sample spectra. The overall signal strength of all sample measurements follow the Fresnel TE transmission and reflection coefficients, so transmittance and reflectance decrease and increase, respectively, as the angle of incidence grows.

The unpatterned sample spectrum serves as a reference spectrum to compare the SHU and photonic crystal samples; it contains oscillations at various incidence angles in the transmission and specular reflection spectra consistent with thin film interference from the QC epilayers (Fig. 6(a), 6(b)).

The photonic/Triangular crystal in this study purely serves as a qualitative comparison sample for anisotropy. This sample displays decreasing transmittance with increasing wavenumbers, while the reflectance spectrum has prominent peaks throughout the entire spectral range. One can also see the strongly varying spectral features with increasing incidence angles for both transmission and reflection (Fig. 6(c), 6(d).) which is expected from the out of plane change of the crystal structure. It is easier to notice this by looking at the shape of each spectrum; the peaks and troughs change, or disappear, as the colors (angles) slowly transition from green to red. The photonic crystal's largest calculated PBG is around 670 cm^{-1}, which lies outside of the detection range of the detector, making it not visible in the spectrum.

Optics EXPRESS

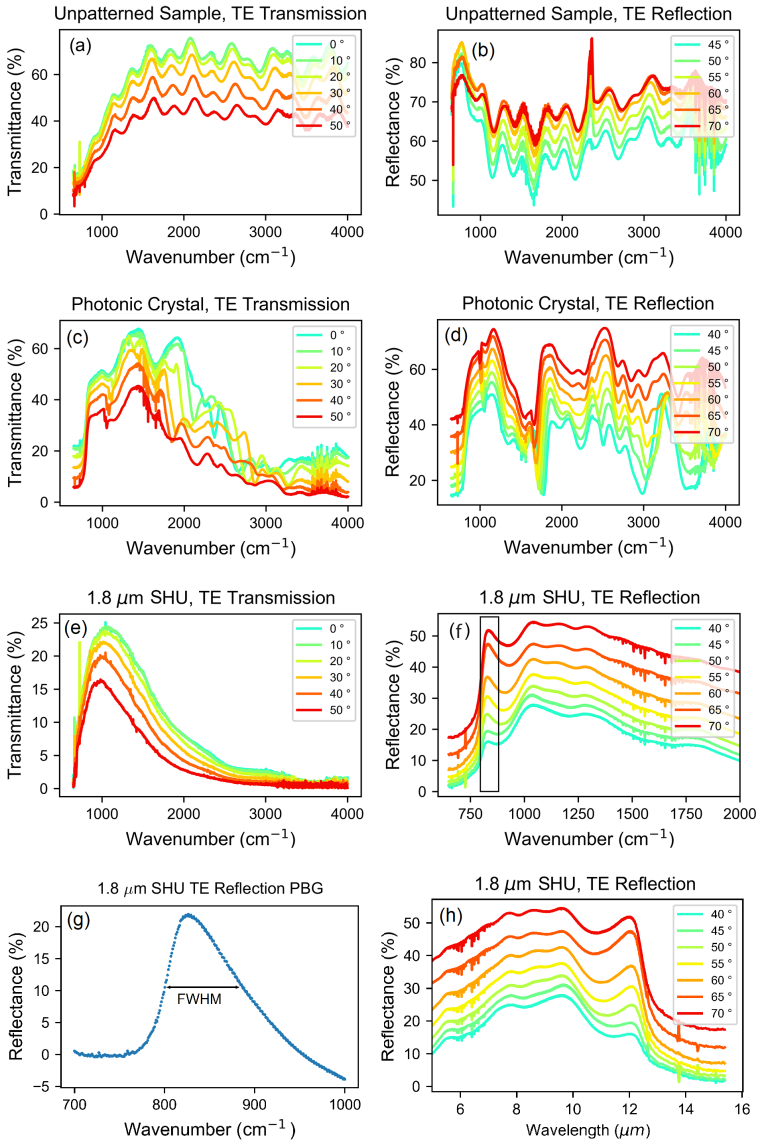

Fig. 6. FTIR spectra of (a,b) the unpatterned sample with QC epilayers, (c,d) the 1.5 μm hole diameter, and a = 3 μm lattice constant photonic crystal sample, and (f,g) the 1.8 μm hole diameter, and 3 μm average point distance SHU sample at varying incidence angles as indicated. The transmittance (a,c,e) and specular reflectance (b,d,f) signals follow the expected behavior of Fresnel TE coefficients with increasing incidence angle. The unpatterned sample shows oscillations from thin film interference, while maintaining an almost identical spectral shape for all incidence angles. The spectral shape of the photonic crystal varies significantly more with increasing incidence angles due to the out of plane change of the crystal structure. The SHU sample exhibits a PBG as an enhanced reflection region around 835 cm^{-1} marked in (f) as a boxed region. Both transmittance and reflectance SHU plots retain their spectral shape in the entire range of incidence angles. (g) shows the measured PBG full width half max (FWHM) from the 70° spectrum in (f); Angles far away from normal incidence will have the largest in plane component and highlight the effect of the PBG. (h) shows the same data in (f), but plotted in terms of wavelength with the PBG around 12.0 μm.

Optics EXPRESS

The 1.8 μm hole diameter with 3 μm average distance SHU sample shows an increased transmission signal at small wavenumbers (700 cm^{-1} - 1500 cm^{-1}) which decreases at growing wavenumbers in both transmission and specular reflection modes; the vanishing signal at large wavenumbers is due to light scattering from the holes (Fig. 6(e), 6(f)). The overall smooth spectral shape is similar for all incidence angles except for where the PBG is located. Reflection spectra show a distinct enhanced reflection region around 835 cm^{-1} corresponding to the SHU PBG in Fig. 6(f); or about 12.0 μm in Fig. 6(h). The measured PBG is close to the predicted one at 810 cm^{-1}; the 3.1% error can be attributed to the imperfect hole surface and patterning, as well as the finite and infinite hole depth from the sample and the simulation, respectively. The 70° spectrum in (f) was modified to remove the background baseline and isolate the PBG; the FWHM is shown in (g). This particular spectrum was selected since light at angles far away from normal incidence couples more to the plane of the SHU structure. The width of the experimentally measured PBG was determined to be 10.4%; bigger than the 7.0% PBG width from simulation.

Furthermore, we tested if our finite SHU structures do, in fact, possess spatial isotropy. The samples were set at a fixed incidence angle of 45° and then rotated from 0° to 180° about their own plane; the in-plane rotational angle spectra for the photonic crystal and the SHU structure are shown in Fig. 7(a) and Fig. 7(b), respectively. The SHU sample conserves its spectral shape throughout the entire range of measured in-plane rotation angles which purely comes from the spatial isotropy. On the other hand, the in-plane rotational angle spectra of the photonic crystal sample show the three-axis symmetry of the hexagonal (or triangular) crystal lattice; most notably measurements in discrete increments of 60° (e.g. 0°, 60°, 120°, 180°) have matching spectral features. The black arrows in Fig. 7(a) point to specific features that only repeat in increments of 60°.

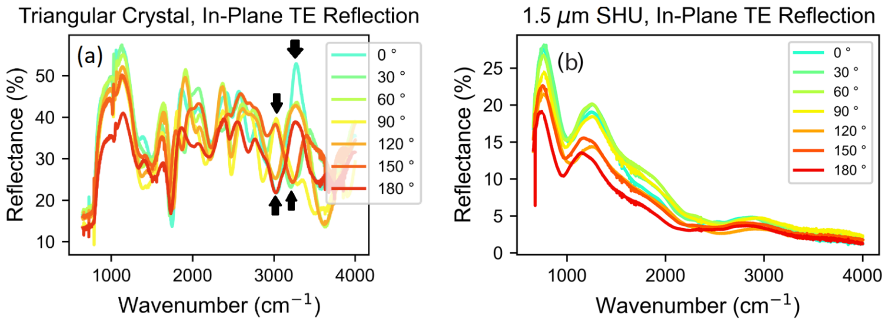

Fig. 7. FTIR spectra of (a) the photonic crystal, and (b) the 1.5 μm SHU sample showing the in-plane reflection of the samples as a function of mount rotation angle at a fixed incidence angle of 45°. The photonic crystal has a different spectral shape at various in-plane rotational angles while the 1.5 μm SHU spectral shape remains the same. This is a clear demonstration of spatial anisotropy from the photonic crystal's three fold symmetry and the spatial isotropy of the SHU structure.

Our spectral analysis shows out of plane transmission and reflection measurements from 0° to large incidence angles (about 70°). Through this approach, we are able to observe the effects of the PBG as an enhanced reflection region that becomes more prominent with growing incidence angle in the 1.8 μm hole diameter with 3 μm average distance SHU sample TE specular reflection measurements shown in Fig. 6(f). The PBG arises from the light impinging onto the surface of the SHU structure which can be separated into individual components; one propagating in the plane of the disordered structure, and the other normal to the structure. The light component propagating in the plane of the SHU structure experiences interference for all in-plane directions, and light is strongly reflected at frequencies matching the PBG frequency. Also, as the angle of incidence increases, so does the magnitude of the in-plane component which results in a larger

Optics EXPRESS

signal at the PBG frequency. To confirm the enhanced reflection signal indeed comes from the disordered holes in the sample, we compare the unpatterned TE specular reflection spectra to the 1.8 μm SHU TE specular reflection spectra. One can see that the signal from the unpatterned sample reflection increases uniformly following Fresnel TE coefficients across the entire range of wavenumbers. On the contrary, the SHU sample reflection signal at the PBG peak increases noticeably more compared to the rest of the of the spectrum at angles far away from normal incidence. Previous work also showed a similar results by peforming out of plane TM spectral measurements on SHU pillar structures. There the authors used a SHU structure with a PBG around 8 μm and 40% width [3].

Lastly, we comment on the fabrication reliability and robustness of the SHU point pattern. The samples fabricated demonstrate consistent reproducibility, as the fabrication techniques used are precise, and well established for these length scales. The tools used in this process allow for lithography patterning accuracy of approximately 800 nm, ensuring high fidelity to GDS design of the SHU structure. Aditionally, the fabrication tolerances achieved result in surface roughness features that are orders of magnitude smaller than the wavelengths of interest in the mid-IR, therefore, not interfering with our measurements of IR spectra. Furthermore, the robustness of the SHU designs is comparable to that of their photonic crystal counterparts. Although SHU patterns are inherently disordered, the precise placement of points is crucial for achieving the desired PBG. If the position of the points shift, the PBG closes up.

7. Conclusion

The motivation for this study stems from classical Fourier optics and the capability of a 4F correlator to extract real-time edge information from an input image. We further motivate this work by showing FDTD simulations of a SHU structure performing edge detection. In this study we have designed, fabricated, and characterized SHU patterned devices for the mid-IR region, and compared them to a reference unpatterned sample as well as a photonic crystal structure. Under TE reflection for the SHU sample, a noticeable band gap around 835 cm^{-1} (λ = 12.0 μm) was detected in the form of an enhanced reflection region with 10.4% PBG width. Furthermore, the SHU in-plane rotational angle measurements showed spatial isotropy from similar spectral shapes, resulting in an in-plane isotropic PBG.

Based on the FDTD simulations, and the experimentally confirmed PBG of the SHU device, our current research is focused on utilizing the SHU pattern as a functional computational metamaterial capable of performing edge detection in the mid-IR range by having the SHU selectively pick diffracted light components associated with the object's edge information, similar to the 4F Fourier correlator built in this study.

Funding. Deutsche Forschungsgemeinschaft (SPP2265).

Acknowledgments. Portions of this work were presented at the International Quantum Cascade Lasers School and Workshop (IQCLSW) in 2024, and at the Conference on Lasers and Electro-Optics (CLEO) in 2024 under the title "Disordered Hyperuniform Metamaterials in the Mid-Infrared".

We would like to thank the Micro and Nano Fabrication Center (MNFC) at Princeton University where the devices were fabricated.

We acknowledge Salvatore Torquato for valuable discussions.

M.A.K. acknowledges funding and support by the Deutsche Forschungsgemeinschaft (DFG, German Research Foundation) through the SPP2265, under grant numbers KL 3391/2-2, WI 5527/1-1 and LO 418/25-1, and by the Initiative and Networking Fund of the Helmholtz Association through the Project "DataMat".

Disclosures. The authors declare no conflicts of interest.

Data Availability. Data underlying the results presented in this paper are not publicly available at this time but may be obtained from the authors upon reasonable request.

References

1. S. Torquato and F. H. Stillinger, "Local density fluctuations, hyperuniformity, and order metrics," Phys. Rev. E **68**(4), 041113 (2003).

Optics EXPRESS

2. S. Torquato, "Hyperuniform states of matter," Phys. Rep. **745**, 1–95 (2018).
3. Y. Zhang, "Novel material engineering in iii-iv semiconductor platforms: Metamaterials with quantum cascade structures," Ph.D. thesis, Princeton University (2022).
4. M. Florescu, P. J. Steinhardt, and S. Torquato, "Optical cavities and waveguides in hyperuniform disordered photonic solids," Phys. Rev. B **87**(16), 165116 (2013).
5. O. Leseur, R. Pierrat, and R. Carminati, "High-density hyperuniform materials can be transparent," Optica **3**(7), 763–767 (2016).
6. W. Man, M. Florescu, K. Matsuyama, *et al.*, "Photonic band gap in isotropic hyperuniform disordered solids with low dielectric contrast," Opt. Express **21**(17), 19972–19981 (2013).
7. L. Dal Negro, *Waves in complex media* (Cambridge University Press, 2022).
8. K. Vynck, R. Pierrat, R. Carminati, *et al.*, "Light in correlated disordered media," Rev. Mod. Phys. **95**(4), 045003 (2023).
9. G. J. Aubry, L. S. Froufe-Pérez, U. Kuhl, *et al.*, "Experimental tuning of transport regimes in hyperuniform disordered photonic materials," Phys. Rev. Lett. **125**(12), 127402 (2020).
10. L. S. Froufe-Pérez, M. Engel, J. J. Sáenz, *et al.*, "Band gap formation and anderson localization in disordered photonic materials with structural correlations," Proc. Natl. Acad. Sci. **114**(36), 9570–9574 (2017).
11. M. Florescu, S. Torquato, and P. J. Steinhardt, "Designer disordered materials with large, complete photonic band gaps," Proc. Natl. Acad. Sci. USA **106**(49), 20658–20663 (2009).
12. M. A. Klatt, P. J. Steinhardt, and S. Torquato, "Wave propagation and band tails of two-dimensional disordered systems in the thermodynamic limit," Proc. Natl. Acad. Sci. **119**(52), e2213633119 (2022).
13. J. D. Joannopoulos, S. G. Johnson, J. N. Winn, *et al.*, *Photonic Crystals: Molding the Flow of Light* (Princeton University Press, Princeton, 2008), 2nd ed.
14. W. Man, M. Megens, P. J. Steinhardt, *et al.*, "Experimental measurement of the photonic properties of icosahedral quasicrystals," Nature **436**(7053), 993–996 (2005).
15. S. Torquato, G. Zhang, and F. H. Stillinger, "Ensemble theory for stealthy hyperuniform disordered ground states," Phys. Rev. X **5**(2), 021020 (2015).
16. O. U. Uche, F. H. Stillinger, and S. Torquato, "Constraints on collective density variables: Two dimensions," Phys. Rev. E **70**(4), 046122 (2004).
17. R. D. Batten, F. H. Stillinger, and S. Torquato, "Classical disordered ground states: Super-ideal gases and stealth and equi-luminous materials," J. Appl. Phys. **104**(3), 033504 (2008).
18. S. Gorsky, W. A. Britton, Y. Chen, *et al.*, "Engineered hyperuniformity for directional light extraction," APL Photonics **4**(11), 110801 (2019).
19. S. Yu, C.-W. Qiu, Y. Chong, *et al.*, "Engineered disorder in photonics," Nat. Rev. Mater. **6**(3), 226–243 (2020).
20. M. M. Milošević, W. Man, G. Nahal, *et al.*, "Hyperuniform disordered waveguides and devices for near infrared silicon photonics," Sci. Rep. **9**(1), 20338 (2019).
21. R. Degl'Innocenti, Y. Shah, L. Masini, *et al.*, "Hyperuniform disordered terahertz quantum cascade laser," Sci. Rep. **6**(1), 19325 (2016).
22. P. M. Piechulla, B. Fuhrmann, E. Slivina, *et al.*, "Tailored light scattering through hyperuniform disorder in self-organized arrays of high-index nanodisks," Adv. Opt. Mater. **9**(17), 2100186 (2021).
23. H. Zhang, H. Chu, H. Giddens, *et al.*, "Experimental demonstration of luneburg lens based on hyperuniform disordered media," Appl. Phys. Lett. **114**(5), 053507 (2019).
24. H. Zhang, Q. Cheng, H. Chu, *et al.*, "Hyperuniform disordered distribution metasurface for scattering reduction," Appl. Phys. Lett. **118**(10), 101601 (2021).
25. N. Tavakoli, R. Spalding, A. Lambertz, *et al.*, "Over 65% sunlight absorption in a 1 μm si slab with hyperuniform texture," ACS Photonics **9**(4), 1206–1217 (2022).
26. M. Merkel, M. Stappers, D. Ray, *et al.*, "Stealthy hyperuniform surface structures for efficiency enhancement of organic solar cells," Adv. Photonics Res. **5**(2), 2300256 (2024).
27. D. Wan, T. Li, S. Chen, *et al.*, "Hyperuniform Disordered Solids with Morphology Engineering," Laser Photonics Rev. **17**(11), 2300398 (2023).
28. S. A. Schulz, R. Oulton, M. Kenney, *et al.*, "Roadmap on photonic metasurfaces," Appl. Phys. Lett. **124**(26), 260701 (2024).
29. C. Guo, M. Xiao, M. Minkov, *et al.*, "Photonic crystal slab laplace operator for image differentiation," Optica **5**(3), 251–256 (2018).
30. Y. Chen, W. A. Britton, and L. Dal Negro, "Hyperuniform scalar random fields for lensless, multispectral imaging systems," Opt. Lett. **46**(21), 5360–5363 (2021).
31. E. Nadernejad, S. Sharifzadeh, and H. Hassanpour, "Edge detection techniques: Evaluations and comparisons," Applied Mathematical Sciences **2**, 1507–1520 (2008).
32. K. Somkantha, N. Theera-Umpon, and S. Auephanwiriyakul, "Boundary detection in medical images using edge following algorithm based on intensity gradient and texture gradient features," IEEE Trans. Biomed. Eng. **58**(3), 567–573 (2011).
33. A. A. Assidiq, O. O. Khalifa, M. R. Islam, *et al.*, "Real time lane detection for autonomous vehicles," in *2008 International Conference on Computer and Communication Engineering*, (IEEE, 2008), pp. 82–88.

Optics EXPRESS

34. A. Singh, M. Singh, and B. Singh, "Face detection and eyes extraction using sobel edge detection and morphological operations," in *2016 Conference on Advances in Signal Processing (CASP)*, (IEEE, 2016), pp. 295–300.
35. D. Ziou and S. Tabbone, "Edge detection techniques-an overview," Pattern Recognition and Image Analysis C/C of Raspoznavaniye Obrazov I Analiz Izobrazhenii **8**(4), 537–559 (1998).
36. S. G. Johnson and J. D. Joannopoulos, "Block-iterative frequency-domain methods for maxwell's equations in a planewave basis," Opt. Express **8**(3), 173–190 (2001).
37. S. Kacmoli, D. L. Sivco, and C. F. Gmachl, "Unidirectional mode selection in bistable quantum cascade ring lasers," Opt. Express **30**(26), 47475–47484 (2022).